

# Single-crystal structure determination of (Mg,Fe)SiO<sub>3</sub> postperovskite

Li Zhang<sup>a,b,1</sup>, Yue Meng<sup>c</sup>, Przemyslaw Dera<sup>d,e</sup>, Wenge Yang<sup>f</sup>, Wendy L. Mao<sup>g,h</sup>, and Ho-kwang Mao<sup>a,b,1</sup>

<sup>a</sup>Center for High Pressure Science and Technology Advanced Research, Shanghai 201203, China; <sup>b</sup>Geophysical Laboratory, Carnegie Institution, Washington, DC 20015; <sup>c</sup>High Pressure Collaborative Access Team, Geophysical Laboratory, Carnegie Institution, Argonne, IL 60439; <sup>d</sup>Center for Advanced Radiation Sources, Argonne National Laboratory, The University of Chicago, Argonne, IL 60439; <sup>e</sup>School of Ocean and Earth Science and Technology, Hawaii Institute of Geophysics and Planetology, Honolulu, HI 96822; <sup>f</sup>High Pressure Synergetic Consortium, Geophysical Laboratory, Carnegie Institution, Argonne, IL 60439; <sup>g</sup>Geological and Environmental Sciences, Stanford University, Stanford, CA 94305; and <sup>h</sup>Photon Science, SLAC National Accelerator Laboratory, Menlo Park, CA 94025

Contributed by Ho-kwang Mao, March 8, 2013 (sent for review February 6, 2013)

Knowledge of the structural properties of mantle phases is critical for understanding the enigmatic seismic features observed in the Earth's lower mantle down to the core–mantle boundary. However, our knowledge of lower mantle phase equilibria at high pressure ( $P$ ) and temperature ( $T$ ) conditions has been based on limited information provided by powder X-ray diffraction technique and theoretical calculations. Here, we report the in situ single-crystal structure determination of (Mg,Fe)SiO<sub>3</sub> postperovskite (ppv) at high  $P$  and after temperature quenching in a diamond anvil cell. Using a newly developed multigrain single-crystal X-ray diffraction analysis technique in a diamond anvil cell, crystallographic orientations of over 100 crystallites were simultaneously determined at high  $P$  in a coarse-grained polycrystalline sample containing submicron ppv grains. Conventional single-crystal structural analysis and refinement methods were applied for a few selected ppv crystallites, which demonstrate the feasibility of the in situ study of crystal structures of submicron crystallites in a multiphase polycrystalline sample contained within a high  $P$  device. The similarity of structural models for single-crystal Fe-bearing ppv (~10 mol% Fe) and Fe-free ppv from previous theoretical calculations suggests that the Fe content in the mantle has a negligible effect on the crystal structure of the ppv phase.

The  $D''$  layer, which represents the lowermost several hundred kilometers of the Earth's mantle, plays a critical role in the dynamics and evolution of our planet's mantle and core. Compositional models suggest that the lower mantle consists mainly of (Mg,Fe)SiO<sub>3</sub> in the perovskite (pv) structure with about 10 mol% Fe (1). MgSiO<sub>3</sub> pv transforms to postperovskite (ppv, CaIrO<sub>3</sub>-type) with the space group Cmcm at the high pressure–temperature ( $P$ – $T$ ) conditions corresponding to the  $D''$  layer (2–4), and the changes associated with the pv–ppv transition may explain several of the intriguing seismic observations of this region (5–7). The in situ determination of the crystal structure of (Mg,Fe)SiO<sub>3</sub> ppv in its stability field will provide key information for understanding the mechanism of the pv–ppv transition and the processes occurring within the  $D''$  layer. Furthermore, compositional changes in (Mg, Fe)SiO<sub>3</sub> may result in subtle changes in the crystal structure of the ppv phase. Recent powder X-ray diffraction (XRD) experiments on ppv with different Fe content suggest that (Mg<sub>0.6</sub>Fe<sub>0.4</sub>)SiO<sub>3</sub> ppv adopts a structure with the Pmcm space group, indicating a structural change in ppv due to Fe-enrichment (8). Precise structure analysis for the ppv phase is required to understand subtle effects of pressure and/or composition on its crystal structure.

Single-crystal XRD provides the most precise structural information that can be used to uniquely determine the space group and structural model. However, preparation of suitable single-crystal ppv samples for conventional single-crystal XRD technique has not been possible. The ppv phase crystallizes into a polycrystalline form at high  $P$ – $T$  conditions and becomes amorphous upon release of pressure back to the ambient conditions (9, 10). Therefore, structural studies of the ppv phase have been limited to powder diffraction techniques. Such powder refinements at extreme  $P$ – $T$  conditions suffer from unreliable intensity measurements

caused by texturing of the sample and spotty diffraction patterns due to crystal growth under high  $T$ . Additionally, the powder refinement quality is significantly affected by overlap of the diffraction peaks, particularly with multiphase samples.

The highly spotty XRD patterns are not ideal for either powder or traditional single-crystal structure determination or refinements, but can be used in a unique analytical approach known as multigrain crystallography (11). While very successful for application to samples at ambient conditions, this method has not been applied for structure determination of samples at high  $P$ . In this study, we synthesized coarse multigrain aggregates of (Mg,Fe)SiO<sub>3</sub> ppv at high  $P$ – $T$  in a diamond anvil cell (DAC), determined the crystallographic orientations of individual ppv crystallites, and then performed single-crystal structure refinement of the (Mg,Fe)SiO<sub>3</sub> ppv crystallites using conventional single-crystal software.

## Synthesis of Submicron-Sized Ppv Crystallites

Synthetic orthopyroxene (opx) with a composition of (Mg<sub>0.85</sub>Fe<sub>0.15</sub>)SiO<sub>3</sub> (En85) was used as the starting material in a Mao-type symmetric DAC for this study. The sample was first compressed into a disk of ~10  $\mu$ m thickness and 40–60  $\mu$ m diameter and placed in a recessed Re gasket sample chamber. Ne was used as a pressure medium and thermal insulation layers for laser heating. Pressures were determined from the diffraction patterns of solid Ne using its known equation of state (12). Angle-dispersive XRD measurements were conducted at 16ID-B of High Pressure Collaborative Access Team (HPCAT) at the Advanced Photon Source (APS), Argonne National Laboratory. High  $P$ – $T$  conditions were achieved by coupling double-sided yttrium lithium fluoride (YLF) laser heating with DAC. To achieve uniform temperature distribution in the sample, we expanded the heating spot to ~30  $\mu$ m flat top and ~55  $\mu$ m full width at half maximum (FWHM). The incident X-ray beam was focused to a  $6 \times 8 \mu\text{m}^2$  FWHM, and XRD patterns of the sample were recorded with a MAR165 CCD.

The En85 sample was initially compressed to 109 GPa at room  $T$  and then heated directly to 2,200–2,400 K. Temperature during laser heating was measured from both sides by spectroradiometry (13). We monitored the growth of crystalline phases at high  $P$ – $T$  conditions with in situ XRD. The ppv phase appeared as a minor phase compared with the pv, and the pressure increased to 111 GPa after  $T$  quenching. We increased the pressure to 118 GPa and conducted prolonged laser heating at 2,300–2,500 K for 30 min to promote the growth of the ppv crystals. Fig. 1A shows a typical XRD pattern collected after  $T$  quenching. The ppv became the

Author contributions: L.Z., W.Y., W.L.M., and H.-k.M. designed research; L.Z. and Y.M. performed research; L.Z., Y.M., P.D., W.Y., and H.-k.M. contributed new reagents/analytic tools; L.Z., Y.M., P.D., W.Y., W.L.M., and H.-k.M. analyzed data; and L.Z., Y.M., P.D., W.Y., W.L.M., and H.-k.M. wrote the paper.

The authors declare no conflict of interest.

<sup>1</sup>To whom correspondence may be addressed. E-mail: lzhang@ciw.edu or mao@gl.ciw.edu.

This article contains supporting information online at [www.pnas.org/lookup/suppl/doi:10.1073/pnas.1304402110/-DCSupplemental](http://www.pnas.org/lookup/suppl/doi:10.1073/pnas.1304402110/-DCSupplemental).

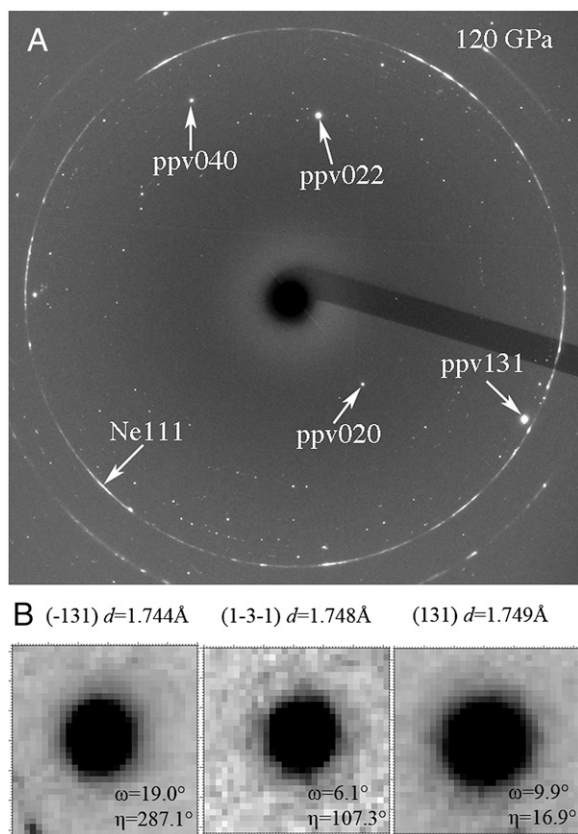


**Fig. 1.** Powder diffraction patterns of  $(\text{Mg,Fe})\text{SiO}_3$  ppv at 120 GPa and after  $T$  quenching. (A) A representative spotty XRD pattern of the ppv sample at a fixed  $\omega$  angle; (B) ROI images of three  $\{131\}$  diffraction spots from one selected single crystallite of the ppv phase.

dominant phase and the pressure increased to 120 GPa. The XRD pattern shows discrete spots instead of continuous Debye rings, indicating the formation of a coarse-grained multigrain aggregate.

Peak fitting of the spotty diffraction peaks from the powder diffraction pattern was performed using PeakFit, and the lattice parameters of the ppv phase were determined by least-squares fit of multiple peak positions as  $a = 2.474$  (3) Å,  $b = 8.106$  (9) Å,  $c = 6.121$  (3) Å, and  $V = 122.8$  Å<sup>3</sup> at 120 GPa and after  $T$  quenching. We mapped individual crystallites across the X-ray beam using the  $300 \times 500$  nm<sup>2</sup> focused polychromatic and monochromatic X-ray beam available at beamline 34ID-E, APS, monitoring the diffraction intensity while moving the sample stage with 500 nm step size. The intensity of the diffraction spot dropped by more than half after moving one step in both directions, indicating that the sizes of crystallites in the sample were  $\sim 0.5$  μm (FWHM) or less.

#### Determination of Crystallographic Orientations of Ppv Crystallites

We aligned the sample to the  $\omega$ -rotation center and collected diffraction patterns in step-scans (2 s/step) with both 0.2° and 1.0° rotation steps over the range of  $\omega$  from  $-26.6^\circ$  to  $24.6^\circ$  at 120 GPa, similar to the “rotation method” used in conventional single-crystal crystallography. Our goal was to index individual crystallites in a polycrystalline sample through determination of orientation matrix of each crystallite. The high brilliance monochromatic X-ray beam available at HPCAT made it possible to record diffraction spots from the coarse polycrystalline sample comprised of up to hundreds of individual submicron crystals at one beam position on the sample. The main challenge in analyzing such data is identification and separation of the signal coming from different

grains into separate subsets, which requires advanced algorithms and computation. The newly developed Fully Automatic Beam-Line Experiments (FABLE) package (11), developed for processing and indexing diffraction spots collected at ambient conditions, was used to determine the crystallographic orientations of individual ppv crystallites in this study. The indexing procedure was carried out using the program GrainSpotter in the FABLE package (11), which we have found to be suitable for processing high  $P$  data. GrainSpotter (14) takes as input a list of measured scattering vectors in reciprocal space ( $G$ -vectors) and a list of theoretical scattering vectors derived from the lattice parameters and space group. The algorithm identifies crystallographic orientations through finding replicas of the set of theoretical scattering vectors in the measured dataset. A different indexing program, ImageD11, has also recently been applied to a high  $P$  DAC data process (15).

The level of difficulty for indexing orientation is proportional to the degree of overlap of the diffraction spots from different crystals. In our sample, and in many other DAC experiments, this problem can be minimized by reducing the sample thickness (a few μm thin samples are normally used in the DAC experimental geometry), promoting crystal growth through prolonged heating, and choosing a proper  $P$ - $T$  path for synthesis. In a well-crystallized ppv sample, the diffraction images are extremely spotty at fixed  $\omega$  positions (Fig. 1A). Single-crystal diffraction peaks occur at very specific rotation angles ( $\omega$ ), and if small rotation steps are used to record individual images, most of the diffraction spots can be treated individually without overlapping with those from neighboring spots in the same XRD pattern. The number of spots appearing in the diffraction images also depends on the relative size between the crystals and the intersection area of X-ray beam and the sample. We were able to study over a hundred crystallites of  $\sim 0.5 \times 0.5$  μm<sup>2</sup> using an X-ray beam slightly larger than  $5 \times 5$  μm<sup>2</sup>.

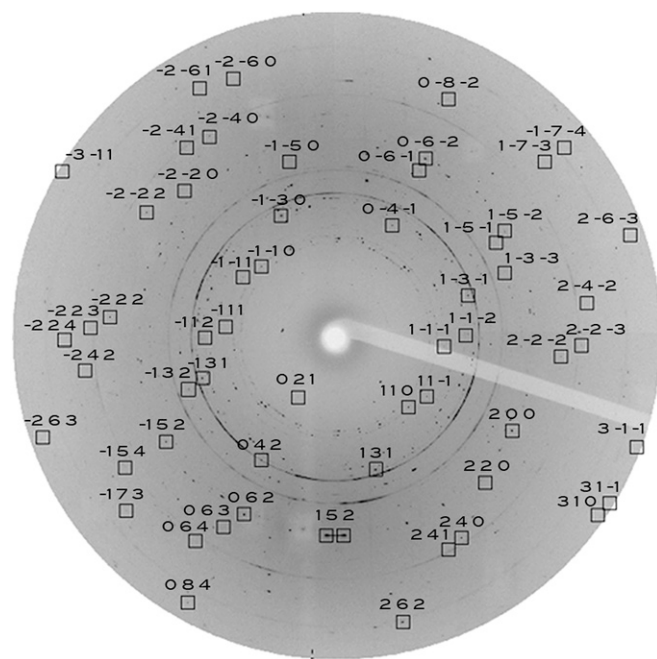


**Fig. 2.** XRD patterns collected in step-scans over the range of  $\omega$  from  $-26.6^\circ$  to  $24.6^\circ$  were merged into a single image after manually masking out the diamond diffraction spots. Black squares indicate positions of observed peaks from one ppv crystallite, and the labels above each square indicate the Miller indices of the peaks. Note that some peaks are too weak to be visible in this intensity scale, but they are clearly visible in individual steps and a narrower range (every  $10^\circ$ ) is merged.

A unique orientation matrix for each crystallite was determined when multiple spots were shown to originate from a single orientation, and indeed these spots were confirmed within the predicted diffraction angles ( $\omega$ ,  $2\theta$ , and  $\eta$ ), where  $\omega$ ,  $\theta$ , and  $\eta$  represent the rotation, Bragg, and azimuth angles, respectively. The matrix of each crystallite was then optimized. More than 100 crystallites belonging to the ppv phase were identified with up to 67 reflections observed in a crystallite using the unit cell parameters obtained from the powder diffraction pattern. Fig. 1B shows the region of interest (ROI) images of three equivalent  $\{131\}$  diffraction spots from one of the crystallites.

The orientation index of individual crystallite allows us to invert all reflections from a known crystallographic orientation and a possible space group. Here, we chose one ppv crystallite as an example. Over a  $\omega$  range from  $-26.6^\circ$  to  $24.6^\circ$ , total 67 reflections were found at  $2\theta < 27^\circ$  for one orientation when the space group  $P222$ , the lowest symmetry in the orthorhombic system, was used to search the spots (Table S1). All of the observed reflections can be assigned to the space group  $Cmcm$ . The given orientation matrix predicts 125 reflections in the same  $\omega$  range based on the space group  $Cmcm$ , resulting in a completeness ratio of 54%. Here, the completeness criterion is defined by the ratio between the observed and expected  $G$ -vectors. All of the missing reflections were blocked by the diamond supporting seats and the rest of the expected reflections were all confirmed by the observations, leading to an actual completeness ratio of 100%.

### Structural Refinement of Single-Crystal Ppv Crystallites

Once diffraction spots were indexed, we selected a few crystallites for structure determination using the conventional single-crystal analysis and refinement methods. The diffraction patterns collected in step-scans over the range of  $\omega$  from  $-26.6^\circ$  to  $24.6^\circ$  were divided into five groups over every  $10^\circ$  and merged into five separate images for the data analysis. A merged image over the whole  $\omega$  range from  $-26.6^\circ$  to  $24.6^\circ$  is shown in Fig. 2, and some peaks were too weak to be visible in this intensity scale. The set of peaks corresponding to one crystallite, identified by FABLE, was exported into GSE\_ADA/RSV software package (16), where peak fitting was performed and appropriate corrections accounting for Lorenz, polarization, DAC absorption, and sample motion effects were applied. The sample motion effects in the beam were corrected using a routine in the GSE\_ADA/RSV package (16) where the differences between the intensity of individual measurement and

**Table 1. Crystal data and structure refinement for one single ppv crystallite**

Parameters	16-IDB, HPCAT, APS
Empirical formula	$Mg_{0.93} Fe_{0.07} SiO_3$
Formula weight	102.50
Pressure	120 (4) GPa
Temperature	293 (2) K
Wavelength	0.37370 Å
Crystal system, space group	Orthorhombic, $Cmcm$
Lattice parameters $a, b, c$ ; Å	2.466(1), 8.130(6), 6.108(10)
Volume	122.5(2) Å <sup>3</sup>
Z, calculated density	4, 5.559 g/cm <sup>3</sup>
Absorption coefficient	1.336 mm <sup>-1</sup>
Crystal size	$\sim 0.5 \times 0.5 \times 0.5 \mu m^3$
Theta range for data collection	3.17–12.76°
Limiting indices	$-2 \leq h \leq 2, -8 \leq k \leq 8, -4 \leq l \leq 4$
Reflections collected/unique	44/25 [R(int) = 0.1379]
Completeness to theta = 12.76	34.7%
Refinement method	Full-matrix least-squares on $F^2$
Goodness-of-fit on $F^2$	1.392
R indices (all data)	R1 = 0.0769, wR2 = 0.2063

**Table 2. Atomic coordinates (multiplied by  $10^4$ ) and equivalent isotropic displacement parameters (Å<sup>3</sup> × 10<sup>3</sup>) for the  $Mg_{0.93} Fe_{0.07} SiO_3$  ppv crystallite**

Atomic coordinates	x	y	z	U(eq)
Mg (1)	0	2,560(16)	2,500	10(6)
Fe (1)	0	2,560(16)	2,500	10(6)
O(2)	0	6,390(40)	4,370(50)	15(8)
O(1)	0	9,290(50)	2,500	22(11)
Si	0	0	0	8(5)

The numbers in parentheses represent standard uncertainties. U(eq) is defined as one-third of the trace of the orthogonalized Uij tensor.

the average of the symmetric reflections were plotted as a function of  $\omega$  rotation angle. In addition, the sample absorption was not taken into account in the corrections because of the high-incident beam energy and negligible sample thickness. Structure refinements were carried out using SHELXL97 (17). We chose three individual ppv crystallites for the structural refinement, and all refinements gave consistent results.

Table 1 provides a summary of the instrument parameters and refinement statistics for the single-crystal structure analysis for one of the ppv crystallites, and Table 2 gives the atomic coordinates and equivalent isotropic displacement parameters from the refinement. The single-crystal diffraction pattern was indexed with an orthorhombic cell with the  $Cmcm$  space group:  $a = 2.466(1)$  Å,  $b = 8.130(6)$  Å,  $c = 6.108(10)$  Å, consistent with the known space group of the Fe-free  $MgSiO_3$  ppv (2). The 44 relatively intense reflections out of 67 were merged into 25 symmetry independents, and statistical parameters indicated good agreement between the observed and calculated structure factors ( $R1 = 7.5\%$  for all peaks). The refinement quality is comparable to the results obtained from one preloaded single crystal in a DAC at moderate  $P$  (18). This result demonstrates the feasibility of studying crystal structures of sub-micron crystallites of high  $P$  phases above Mbar pressure range.

This represents a single-crystal structure refinement of  $(Mg,Fe)SiO_3$  ppv. Table 3 lists the selected bond lengths and interatomic angles in the structure of ppv at high  $P$  and room  $T$  in comparison with the results from powder diffraction data in  $(Mg_{1-x}Fe_x)SiO_3$  ( $0 \leq x \leq 0.1$ ) (2, 8, 10, 19). The Fe content in the ppv phase was refined to be  $x = 0.07$  when the Fe–Mg ratio was used as a variable in the refinement. At 120 GPa and after  $T$  quench, ppv is the dominant phase and the volume difference between the coexisting pv and ppv is 1.1%, comparable to the volume difference 1.0–1.2% in  $MgSiO_3$  (2). This indicates undistinguishable Fe partitioning between the pv and ppv phases as evidenced from the XRD data. With  $(Mg_{0.85}Fe_{0.15})SiO_3$  as the starting material, we estimate the Fe content in the ppv phase is  $x = 0.1 \pm 0.05$ . The

**Table 3. Selected bond lengths (Å) and interatomic angles (°) in the single-crystal ppv structure at 120 GPa and room  $T$  in comparison with results from previous powder diffraction data for  $(Mg_{1-x}Fe_x)SiO_3$**

Parameters	Single crystal	Powder (ref. 8)	Powder (ref. 10)	Theory (ref. 2)	Powder (ref. 19)
Formula (x)	0.07	0.1	0.09	0	0
$P$ (GPa)	120(4)	131	126(2)	121	116
$T$ (K)	300	300	300	300	300
Si–O1×2	1.63(2)	1.62	1.66(1)	1.64	1.61
Si–O2×4	1.72(2)	1.73	1.71(2)	1.66	1.72
Mg–O1×2	1.87(3)	1.85	1.85(3)	1.84	1.95
Mg–O2×4	1.93(2)	1.95	1.88(2)	1.94	1.95
Mg–O2×2	2.09(3)	2.01	2.15(3)	2.13	2.07
$\angle SiO1Si$	139(3)	141	134(2)	138	146
$\angle SiO2Si$	92(1)	91	92(2)	94	92

crystal structure of the ppv phase is in good agreement with the structures obtained from powder diffraction data of  $(\text{Mg}_{0.9}\text{Fe}_{0.1})\text{SiO}_3$  ppv (8, 10) and theoretical calculations of  $\text{MgSiO}_3$  ppv (2). The various model compositions provided a consistent Fe content of  $\sim 10$  mol% for the bulk composition in the mantle (1). The consistency of the structural parameters between the Fe-bearing ppv in our experiments and the Fe-free ppv from the theoretically calculated structural model (2) suggests that the Fe content in the mantle has a negligible effect on the crystal structure of the ppv phase, in agreement with the previous theoretical calculations suggesting a minor effect of 6.25 mol% Fe content on the thermodynamic properties of the ppv phase at  $P$ - $T$  conditions of the lowermost mantle (20). However, if the ultralow-velocity zones at the very base of the lower mantle are highly enriched in Fe from reacting with the core (6), the ppv phase might alter its space group from  $\text{Cmcm}$  to  $\text{Pmcm}$  depending on the degree of Fe enrichment (8). Structures from powder diffraction are typically less accurate than those from single crystals. This first single-crystal structure model of Fe-bearing ppv provides a reliable reference for structure studies using other approaches. Furthermore, the precise structural information of submicron-grained single-crystal ppv allows us to separate the effects from composition, pressure, and/or sample quality on the structure of ppv above Mbar pressure.

Multigrain crystallography with synchrotron radiation at high  $P$  shows a number of advantages compared with powder diffraction

because single-crystal diffraction provides rigorous 3D angular and symmetric relations based on reliable intensity measurements. The capability of indexing aggregates of up to several hundred submicron crystallites and performing structure analysis of each crystallite within a DAC allows for in situ single-crystal studies under previously inaccessible high  $P$  conditions. Single-crystal structure analysis above Mbar pressure is no longer limited to a few instances where a compound forms as a single-crystal under high  $P$  condition.

**ACKNOWLEDGMENTS.** We thank A. Kyono for his helpful discussions and S. Merkel for introducing us to the indexing software. This research was supported by National Science Foundation (NSF) Grants EAR-0911492, EAR-1055454, and EAR-1119504. High Pressure Synergetic Consortium (HPSynC) is supported as part of EFree, an Energy Frontier Research Center funded by the US Department of Energy (DOE)–Office of Basic Energy Sciences (BES) under Grant DE-SC0001057. Most of the experiments were performed at HPCAT (Sector 16) of APS. HPCAT is supported by the Carnegie Institution of Washington, the Carnegie/Department of Energy Alliance Center, the University of Nevada, Las Vegas, and Lawrence Livermore National Laboratory through funding from the DOE National Nuclear Security Administration, the DOE Office of Science, and BES, with the undulator upgrade supported by NSF MRI-1126249. Portions of this work were performed at the 34IDE beamline, APS. Use of the APS facility was supported by DOE–BES under Contract DE-AC02-06CH11357.

1. McDonough WF, Sun S-s (1995) The composition of the Earth. *Chem Geol* 120(3-4): 223–253.
2. Murakami M, Hirose K, Kawamura K, Sata N, Ohishi Y (2004) Post-perovskite phase transition in  $\text{MgSiO}_3$ . *Science* 304(5672):855–858.
3. Oganov AR, Ono S (2004) Theoretical and experimental evidence for a post-perovskite phase of  $\text{MgSiO}_3$  in Earth's D" layer. *Nature* 430(6998):445–448.
4. Tsuchiya T, Tsuchiya J, Umamoto K, Wentzcovitch RM (2004) Phase transition in  $\text{MgSiO}_3$  perovskite in the earth's lower mantle. *Earth Planet Sci Lett* 224(3-4):241–248.
5. Duffy TS (2008) Mineralogy at the extremes. *Nature* 451(7176):269–270.
6. Mao WL, et al. (2006) Iron-rich post-perovskite and the origin of ultralow-velocity zones. *Science* 312(5773):564–565.
7. Garnero EJ, McNamara AK (2008) Structure and dynamics of Earth's lower mantle. *Science* 320(5876):626–628.
8. Yamanaka T, et al. (2012) Crystal structures of  $(\text{Mg}_{1-x}\text{Fe}_x)\text{SiO}_3$  postperovskite at high pressures. *Proc Natl Acad Sci USA* 109(4):1035–1040.
9. Shieh SR, et al. (2006) Equation of state of the postperovskite phase synthesized from a natural  $(\text{Mg,Fe})\text{SiO}_3$  orthopyroxene. *Proc Natl Acad Sci USA* 103(9):3039–3043.
10. Shim SH, et al. (2008) Crystal structure and thermoelastic properties of  $(\text{Mg}_{0.91}\text{Fe}_{0.09})\text{SiO}_3$  postperovskite up to 135 GPa and 2,700 K. *Proc Natl Acad Sci USA* 105(21): 7382–7386.
11. Sørensen HO, et al. (2012) Multigrain crystallography. *Z Kristallogr* 227(1):63–78.
12. Fei Y, et al. (2007) Toward an internally consistent pressure scale. *Proc Natl Acad Sci USA* 104(22):9182–9186.
13. Meng Y, Shen G, Mao H-k (2006) Double-sided laser heating system at HPCAT for in situ x-ray diffraction at high pressures and high temperatures. *J Phys: Condens Matter* 18:S1097–S1103.
14. Schmidt S (2010) *GrainSpotter v. 0.82* (Riso National Laboratory for Sustainable Energy, Technical University of Denmark, Roskilde, Denmark).
15. Nisr C, et al. (2012) High resolution three-dimensional X-ray diffraction study of dislocations in grains of  $\text{MgGeO}_3$  post-perovskite at 90 GPa. *J Geophys Res* 117(B3): B03201.
16. Dera P (2007) *GSE-ADA Data Analysis Program for Monochromatic Single Crystal Diffraction with Area Detector* (GeoSoilEnviroCARS, Argonne, IL).
17. Sheldrick GM (2008) A short history of SHELX. *Acta Crystallogr A* 64(Pt 1):112–122.
18. Dera P, Lazarz JD, Prakapenka VB, Barkley M, Downs RT (2011) New insights into the high-pressure polymorphism of  $\text{SiO}_2$  cristobalite. *Phys Chem Miner* 38(7):517–529.
19. Ono S (2006) Equation of state of  $\text{CaIrO}_3$ -type  $\text{MgSiO}_3$  up to 144 GPa. *Am Mineral* 91(2-3):475–478.
20. Metsue A, Tsuchiya T (2011) Lattice dynamics and thermodynamic properties of  $(\text{Mg,Fe}_{2+})\text{SiO}_3$  postperovskite. *J Geophys Res* 116(B8):B08207.